Aeroacoustics Conferences
June 14-17, 2022, Southampton, UK
28th AIAA/CEAS Aeroacoustics 2022 Conference

10.2514/6.2022-2918

Towards Wall-Modeled LES with Lattice Boltzmann Method for Aeroacoustics: Application and Understanding

Malav Soni*, Roland Ewert† and Jan Delfs‡
DLR Institute for Aerodynamics and Flow Technology, Dep. of Technical Acoustics, Lilienthalplatz 7, 38108 Braunschweig

Kannan Masilamani§
DLR Institute of Software Methods for Product Virtualization, Zwickauer Straße 46, 01069 Dresden

The aim of this work is direct noise computation (DNC) of high-lift wing using Wall-modeled LES (WMLES) with Lattice Boltzmann Method (LBM). There are two aspects of this work: application, where the commercial LB solver ProLB is used as a DNC tool to compute high-lift noise, and understanding, where an effort is made to gather know-how about the intricate details/nuances involved with wall-modeling in LBM by implementing it. For the present study, the Category 6 LEISA2 F16 high-lift configuration from the Benchmark for Airframe Noise Computations (BANC) workshop has been selected as the high-lift airfoil. The three-element unswept high-lift wing with deployed slat and flap is resolved on a mesh with different spanwise resolutions ranging from 5% to 20% clean chord length. Periodic boundary condition is used along the spanwise direction. The results of WMLES-LBM simulations were validated for relative accuracy against the extensive experimental BANC database. Results of both aerodynamic and aeroacoustic comparison with the experiments is discussed in detail. For the aspect of understanding, a quasi-analytical wall function for flat walls has been introduced into the academic LB research code Musubi. Turbulent channel flow at Re_τ=1000 was chosen as test-case for the validation. Results of the simulation were compared with the published DNS results.

I. Introduction

AIRFRAME noise is generated during the take-off and approach phase by the interaction of the complex flow with the deployed landing gear and high-lift devices (slat and flap). During the approach phase the airframe noise represents the dominant noise contribution [1]. It becomes imperative to reduce this source of noise in order to meet the future stringent noise limits. Different approaches to predict this type of noise source have been listed in reference [2].

Flow field that develops around the high lift devices is quite complex and highly unsteady [3]. Complexity of the flow field is associated with several flow phenomena i.e. generation and interaction of shear layers, impingement of shear layer vortices, flow re-circulation and separation etc. Accurate prediction of the unsteady flow features is the aim of scale-resolving flow simulations such as Large-Eddy Simulation (LES). DNC of high-lift device noise aims at simulating simultaneously the unsteady turbulent flow with the sound generation and propagation process as a part of one simulation. Particularly, we are interested in the high-lift devices at approach that involve flow Reynolds number of $O(10^6 - 10^7)$. Wall resolved LES (WRLES) requires full resolution of the inner layer physics inside the Turbulent boundary layer (TBL). Computational expense incurred for WRLES at technical relevant high Reynolds numbers is not economical even with the current computing power [4].The grid point requirement for the WRLES scales as $Re^{13/7}$ and for WMLES which models the physics of the inner layer, it scales as Re^1 [5]. Since the inner layer is modeled, only the outer layer of the Turbulent Boundary Layer (TBL) is resolved with LES. This significantly reduces the computational expense.

In recent years, LBM has gained popularity for subsonic, high Reynolds number aerodynamic flows. It is inherently an unsteady method with a good computational efficiency [6] for high fidelity LES computation. Cartesian grids with

*Research scientist
†Senior scientist, AIAA Senior member
‡Head of the department, AIAA Senior member
§Research scientist

LBM enable a quick meshing approach for any complex type of geometry. Because of its low dissipative nature, LBM facilitates the aeroacoustic application. Considering the isotropic nature of mesh, WRLES on hierarchical Cartesian meshes become too expensive for industrial applications. Usage of wall models mitigates this issue [7], [8]. In the present work WMLES in combination with LBM is used to simulate high-lift noise. Studies for high-lift noise with Very Large-Eddy Simulation (VLES-)/WMLES-LBM have been reported using PowerFLOW software [9]-[11] . In the present work, ProLB v2.6.3 has been chosen for the simulation of the high-lift noise.

For the application part, DLR/ONERA F16 geometry is used as the high-lift wing for simulation with ProLB, see figure 3. This geometry has been extensively studied experimentally within the joint ONERA/DLR project LEISA2 [13]. Several high-lift noise studies with continuum based solvers have been carried out with F16 geometry. These studies used different approaches like: zonal hybrid Reynolds-averaged Navier-Stokes (RANS)/LES [30], global hybrid RANS/LES [31], WRLES [32] and perturbation based approaches i.e. Forced Eddy Simulation (FES) [33] and Overset-LES (OLES) [34]. To the authors knowledge, this is the first high-lift noise study with F16 geometry using WMLES-LBM. In this study, ProLB is indeed used as a DNC tool by directly resolving the acoustics in the far-field.

For the second part of the study, the academic research LB software Musubi is utilized to simulate a turbulent channel flow problem at wall shear stress velocity based Reynolds number $Re_\tau = 1000$. The canonical turbulent flow problem is selected to study aspects of the wall model implementation.

The paper is organized as follows: First, Sec. II describes the LBM theory. Sec. III describes the numerical set-up details and results of High-lift noise simulation. After that Sec. IV describes the numerical set-up details and results of the turbulent channel flow (TCF) simulation.

II. Numerical method

A. Lattice Boltzmann scheme

In this study Lattice Boltzmann method has been used for the fluid flow and acoustics simulation. This approach is based upon the Boltzmann equation which describes the dynamics of fluid on a mesoscopic scale. The fundamental variable for the Boltzmann equation is the particle distribution function $f = f(\boldsymbol{x}, \boldsymbol{\xi}, t)$ that represents the particle density/probability of finding particles with microscopic particle velocity $\boldsymbol{\xi} = (\xi_x, \xi_y, \xi_z)$ at a given time t and at a position $\boldsymbol{x}$. The force-free Boltzmann equation (dimensional) describes the evolution of f in time as a result of advection and collision:

$$\frac{\partial f}{\partial t} + \boldsymbol{\xi}.\frac{\partial f}{\partial \boldsymbol{x}} = \Omega(f), \tag{1}$$

where $\Omega(f)$ - is the collision operator which locally redistributes f. The macroscopic quantities of interest i.e. density, momentum are obtained from the moments of f over all the particle velocities $\boldsymbol{\xi}$:

$$\begin{aligned} \rho(\boldsymbol{x}, t) &= \int f d\boldsymbol{\xi}, \\ \rho(\boldsymbol{x}, t)\boldsymbol{u}(\boldsymbol{x}, t) &= \int f \boldsymbol{\xi} d\boldsymbol{\xi}. \end{aligned} \tag{2}$$

Analogous to eq. (1) , the lattice Boltzmann equation (LBE) describes the dynamics of the discrete particle distribution functions f_i, also referred to as particle populations[15], where i in f_i is associated with the chosen discrete set of particle velocities $\{\boldsymbol{\xi}_i = (\xi_{ix}, \xi_{iy}, \xi_{iz})\}$. Now, the macroscopic quantities are obtained from the sum of the particle populations over a discrete set of N particle velocities:

$$\rho(\boldsymbol{x}, t) = \sum_{i=0}^{N-1} f_i(\boldsymbol{x}, t), \quad \rho(\boldsymbol{x}, t)\boldsymbol{u}(\boldsymbol{x}, t) = \sum_{i=0}^{N-1} \boldsymbol{\xi}_i f_i(\boldsymbol{x}, t). \tag{3}$$

Discretisation of eq. (1) in velocity space is carried out by truncating the Hermite series expansion of f on the basis of the Hermite polynomials in velocity space. Later on, using the Gauß-Hermite quadrature, the integral form of moments (eq. (2)) can be written as the summation over a specific set of velocities [16]. Choice of the discrete particle velocity set $\{\boldsymbol{\xi}_i\}$ determines the lattice. Our studies used a regular D3Q19 (19 velocities in 3 dimensions) lattice that will arrange the nodes in a cubic fashion and on each node 19 $f_i's$ are stored. Figure 1 shows a D3Q19 lattice, where each node is connected to its neighboring node with a discrete velocity link. Eq.(1) when discretized in the velocity space, physical

space and time gives us the Lattice Boltzmann equation (LBE) as shown in eq. (4).

$$f_i(\boldsymbol{x} + \boldsymbol{\xi}_i \Delta t, t + \Delta t) = f_i(\boldsymbol{x}, t) + \Omega_i(\boldsymbol{x}, t) \tag{4}$$

where Δt is the time step and Ω_i is the collision operator.

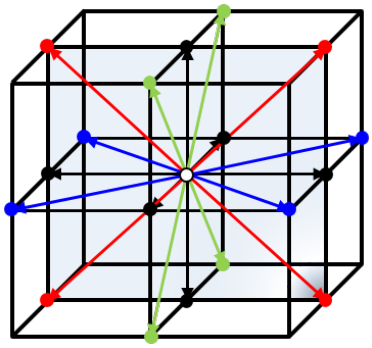

Fig. 1 D3Q19 stencil.

In the LB algorithm, the $f_i's$ on the lattice are updated in time via two steps: collision and streaming. The collision step is local and its role is to instantaneously redistribute the particles/$f_i's$ among the different particle/discrete velocities as:

$$f_i{}^c(\boldsymbol{x}, t) = f_i(\boldsymbol{x}, t) + \Omega_i(\boldsymbol{x}, t), \tag{5}$$

where $f_i{}^c$ represents the post-collision particle population. The streaming step involves the propagation of this $f_i{}^c$ to the neighboring lattice node along its post-collision velocity direction as:

$$f_i(\boldsymbol{x} + \boldsymbol{\xi}_i \Delta t, t + \Delta t) = f_i{}^c(\boldsymbol{x}, t). \tag{6}$$

Flow physics is introduced through modeling of the collision operator. The simple Bhatnagar-Gross-Krook (BGK) collision operator is used to model $\Omega_i(\boldsymbol{x}, t)$ as:

$$\Omega_i(\boldsymbol{x}, t) = -\frac{\Delta t}{\tau}(f_i(\boldsymbol{x}, t) - f_i{}^{eq}(\boldsymbol{x}, t)) \tag{7}$$

which corresponds to the relaxation of the particle populations towards their respective equilibrium state $f_i{}^{eq}$ with a prescribed relaxation time τ. The discrete equilibrium distribution function $f_i{}^{eq}$ is given by the truncated Hermite series expansion, normally at the second order, of the continuous Maxwell-Boltzmann distribution (f^{eq}) as:

$$f_i^{eq}(\rho, \boldsymbol{u}) = w_i \rho \left(1 + \frac{\xi_{i\alpha} u_\alpha}{a_0^2} + \frac{u_\alpha u_\beta (\xi_{i\alpha}\xi_{i\beta} - a_0^2 \delta_{\alpha\beta})}{2a_0^4}\right) + O(Ma^3), \tag{8}$$

where a_0 is the constant speed of sound, w_i are the weights for each discrete velocity that are specific to a lattice. The relaxation time is unique for different flow configurations as it is obtained using the kinematic viscosity $\boldsymbol{\nu}$ and a_0 as: $\tau/\Delta t = 1/2 + \nu/a_0^2 \Delta t$. Reduced description of f and f^{eq} is sufficient enough to recover the correct macroscopic conservation laws [16]. The pressure is computed using the iso-thermal equation of state as: $p = a_0^2 \rho$. Using the BGK collision operator, eq. (4) can be rewritten as the LB-BGK equation as:

$$f_i(\boldsymbol{x} + \boldsymbol{c}_i \Delta t, t + \Delta t) = f_i(\boldsymbol{x}, t) - \frac{\Delta t}{\tau}(f_i(\boldsymbol{x}, t) - f_i^{eq}(\boldsymbol{x}, t)). \tag{9}$$

The non-equilibrium population, f_i^{neq}, is denoted as the deviation from the equilibrium:

$$f_i^{neq} = f_i - f_i^{eq}. \tag{10}$$

The use of the BGK scheme was strictly restricted for explaining the LB scheme. This simple form of approximation for the collision operator suffers from stability issues at higher Reynolds number. Since we are interested in simulating highly turbulent flows, details of the key aspects i.e. collision scheme used in ProLB and Musubi will be given in the subsequent sections.

B. ProLB: Key ingredients

ProLB [17] is an industrial LB solver that is developed within a scientific consortium including CS GROUP, Renault, Airbus, Ecole Centrale de Lyon, Aix-Marseille University It is a cell-vertex based solver that deploys a D3Q19 lattice. ProLB version 2.6.3 was used in this study.

1. Collision scheme

To ensure superior stability at higher Reynolds number a Hybrid Recursive Regularized Bhatnagar-Gross-Krook (HRR-BGK) [18] collision scheme is used instead of simpler BGK form. The populations $f_i's$ are regularized, refer [18], before the collision step. The collision operator in this scheme look like:

$$\Omega_i = -\frac{\Delta t}{\tau} {f_i}^{neq}. \tag{11}$$

Here the non-equilibrium population is computed in an hybrid fashion as:

$${f_i}^{neq} = \sigma_{HRR} {f_i}^{neq,LB} + (1 - \sigma_{HRR}) {f_i}^{neq,FD} \tag{12}$$

where

$$\begin{aligned} {f_i}^{neq,LB} &= \frac{Q_{i\alpha\beta}}{2a_0^4} \sum_{\alpha} \xi_{i\alpha}\xi_{i\beta}(f_i - f_i^{eq}), \\ {f_i}^{neq,FD} &= -\frac{\tau\rho\omega_i}{2\Delta t a_0^2} Q_{i\alpha\beta} \left(\frac{\partial u_\alpha}{\partial x_\beta} + \frac{\partial u_\beta}{\partial x_\alpha} \right) \end{aligned} \tag{13}$$

with $Q_{i\alpha\beta} = \xi_{i\alpha}\xi_{i\beta} - a_0^2\delta_{\alpha\beta}$ and $\sigma_{HRR} = 0.98$. To compute the velocity gradients in ${f_i}^{neq,FD}$, second order centered finite differences are used . Non-hydrodynamic contribution which is responsible for generating spurious noise at the fine to coarse mesh interface is effectively damped by this scheme [19].

2. Turbulence model

In the LB framework, LES is embedded directly by replacing the kinematic viscosity with an effective viscosity. The effective viscosity is expressed as a sum of kinematic and turbulent viscosity: $\nu_{eff} = \nu + \nu_{turb}$. Here ν_{turb} accounts for the contribution of the unresolved scales in the bulk flow. Shear Improved Smagorinsky (SISM) [21] model, which is an improvement over the classical Smagorinsky model, provides the ν_{turb} as follows:

$$\nu_{turb} = (C_s\Delta x)^2 \left(|\boldsymbol{S}|(\boldsymbol{x}, t) - \tilde{S}(\boldsymbol{x}, t)\right), \tag{14}$$

where $C_s = 0.18$ is the smagorinsky constant, Δx is the lattice spacing, $|\boldsymbol{S}|$ is the norm of the strain rate tensor and $\tilde{S}$ is the low-pass filtering of rate of strain. Instead of kinematic viscosity, now an effective viscosity enters the relaxation parameter:

$$\frac{\tau}{\Delta t} = \frac{1}{2} + \frac{\nu_{eff}}{a_0^2 \Delta t}. \tag{15}$$

3. Wall model

A logarithmic wall function, eq. (16), is used to model the dynamics of turbulence at the first off-wall cell with extra correcting terms for the adverse pressure gradient, the curvature correction and near-wall damping [20].

$$u^+(y^+) = \left(\frac{1}{k}\ln(y^+) + B + F_p(y^+) + F_c(y^+)\right) F_d(y^+) \tag{16}$$

with

$$u^+ = \frac{u}{u_\tau}, \quad y^+ = \frac{y u_\tau}{\nu}, \quad u_\tau = \sqrt{\frac{\tau_w}{\rho}}, \tag{17}$$

where u_τ is the friction velocity, τ_w is the wall shear stress, $F_p(y^+)$, $F_c(y^+)$ and $F_d(y^+)$ - are the adverse pressure, the curvature correction and near wall damping correcting terms, the von-Karman constant $k = 0.41$ and constant $B = 5.2$.

C. Musubi: Key ingredients

Musubi [22] is a parallel multi-level LB solver initially developed in Simulation Techniques and Scientific (STS) Computing Group, University of Siegen. It allows for the simulation of different flow physics i.e. weakly compressible, multi-component flows etc. The code is now developed further for high Reynolds number and aeroacoustic applications i.e. utilizing wall models and advanced collision schemes. It is a cell-centered octree based solver. The octree meshes are created using the mesh generator Seeder from STS.

1. Collison scheme

A multi-relaxation time (MRT), see d'Humières [23], collision scheme is used for high Reynolds number simulations. In this scheme, first the populations are transformed in to the moment space using a linear transformation. Instead of populations, these moments are relaxed towards their equilibrium using individual relaxation times. Post-collision moments are than transformed back to the population space and streamed further. This approach increases stability since it allows to relax each moment independently, especially the higher order non-hydrodynamic moments [24].

2. Turbulence model

In this work, VREMAN [25] model is used to provide the contribution of the unresolved scales, ν_{turb}. It uses strain rate and vorticity rate tensor for the computation of ν_{turb} as:

$$\nu_{turb} = c_v(\Delta x)^2 \left(\sqrt{\frac{B_\beta}{\alpha_{ij}\alpha_{ij}}}\right), \tag{18}$$

where

$$B_\beta = \beta_{11}\beta_{22} - \beta_{12}^2 + \beta_{11}\beta_{33} - \beta_{13}^2 + \beta_{22}\beta_{33} - \beta_{23}^2, \tag{19}$$

$$\beta_{ij} = \alpha_{mi}\alpha_{mj}, \tag{20}$$

$$\alpha_{ij} = \frac{\partial u_j}{\partial x_i}. \tag{21}$$

α_{ij} is the resolved velocity gradient. The model constant c_v is related to the Smagorinsky constant C_s by $c_\nu \approx 2.5C_s^2$. The contribution from ν_{turb} enters the relaxation time in the similar fashion as shown in eq. (15).

3. Wall model

Since we use uniform Cartesian meshes, isotropic mesh refinement in the near wall region could easily result in large number of overall mesh points for the high Reynolds number cases. Such an issue can be avoided by using a wall model which will predict the velocity and friction velocity in the first off-wall point. As a part of understanding LBM as a DNC tool, developing and understanding of wall-modeling in the LBM framework, besides the numerics of LBM, is of prime importance. Recently an algebraic type wall model based on the concept of Malaspinas et al. [26] was introduced in Musubi. This initial implementation is applicable only for the flat walls which implies that the distance of the first and second off-wall nodes from the wall is fixed, see figure 2. In this case, the first off-wall node distance is $0.5\Delta x$ and the second off-wall node distance is $1.5\Delta x$ away from the wall. Basic idea of this wall model is to replace the no-slip boundary condition by imposing a tangential velocity component (macroscopic) at the first off-wall node using analytical/quasi-analytical wall functions. Under the assumption that the second off-wall node lies in the inner TBL, the velocity information available at the second off-wall node from the bulk flow is utilised to compute the u_τ from the wall function. Using this u_τ the tangential velocity can be obtained at the first off-wall node. Explicit (Werner & Wengle [28]) and implicit wall functions (Musker, Reichardt etc. see Ref. [26]) were implemented. The test-case computed with this wall model used Musker wall function (eq. (22)) to model the inner TBL. The implicit wall functions were solved iteratively using the fixed point iteration method.

$$u^+ = 5.424 \arctan\left(\frac{2.0y^+ - 8.15}{16.7}\right) + \log_{10}\left(\frac{(y^+ + 10.6)^{9.6}}{(y^{+2} - 8.15y^+ + 86.0)^2}\right) - 3.5072790194 \tag{22}$$

On the contact side with the boundary, the first off-wall nodes have a missing fluid neighbour node. The distribution functions in the direction of the missing neighboring nodes are unknown. Thus, at the first off-wall nodes a particular

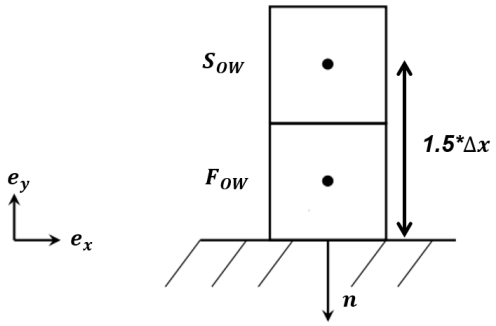

Fig. 2 Model arrangement (2D) of the nodes for wall model concept. F_{OW}, S_{OW}**- first & second off-wall nodes.**

treatment is required to properly account for the distribution functions virtually coming from inside the boundary. Several ways of treating this issue are reported in literature [26] out of which we chose reconstruction of all distributions at the first off wall nodes. The distribution functions at the first off-wall nodes are computed as: ${f_i}^{eq} + {f_i}^{neq}$. Density ρ and ${f_i}^{neq}$ at the first off-wall nodes are obtained via the zeroth-order extrapolation from the neighboring fluid node. The equilibrium part ${f_i}^{eq}$ at first off-wall node is computed using the macroscopic density and imposed velocity from the wall function.

III. High-lift simulations

A. Configuration

High-lift wing under consideration is the widely utilised DLR/ONERA F16 geometry. Under the joint DLR/ONERA project LEISA2 [13], extensive experimental studies are carried out with this geometry. The experimental aerodynamic and aeroacoustic database is co-owned by ONERA and DLR but recently the database is also made public under the framework of the Benchmark for Airframe Noise Computation (BANC) [14] (category 6). The F16 geometry has a unswept, three-element configuration with slat and flap deployed at 27.834 and 35.011 deg, respectively. It has a clean chord length $c = 0.3$ m and spanwise extent $L_z = 0.8$ m. Slat chord length is 0.0558 m. Figure 3 shows the section of the F16 geometry. The axis origin of the F16 geometry is at the leading edge of the slat when the slat is in retracted position. Free-field flow conditions chosen for this study are: free-stream inflow velocity $U_\infty = 61.53$ m/s, free-stream Mach number $M_\infty = 0.18$ and angle of attack $\alpha = 6.15$ deg. Reynolds number based on the clean chord and the kinematic viscosity for air, $\nu = 1.49e{-}05\ m^2/s$, is $Re_c \simeq 1,230,000$. Measurements were carried out in the ONERA's F2 (closed wall) aerodynamic wind tunnel and DLR's AWB (open-jet) aeroacoustic wind tunnel. Detailed description of the experimental methodology and the results are discussed in Ref. [13].

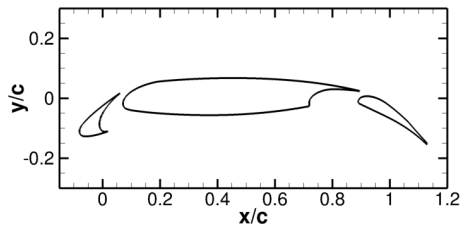

Fig. 3 DLR F16 profile.

For the near-field results comparison, the experimental data from F2 tunnel will be used and for the far-field acoustic propagation results comparison, the data from AWB tunnel will be used.

B. Numerical setup

Square shaped computational domain as shown in figure 4a) is used for the simulation. F16 geometry is arranged in the middle of the domain and the domain extends from the axis origin of the geometry by 50c in both streamwise (X-axis) and wall normal (Y-axis) direction. Green slab in figure 4a) represents the location of velocity inlet boundary and the other three blue slabs the location of the outlet boundary. Transients resulting from the flow initialisation get reflected at the boundaries and in order to damp them, sponge zones are placed near the boundaries. The sponge zones stretch inwards from the boundaries in to the fluid domain by 3c. Wall boundary condition was applied on the surfaces of all three elements of the F16 geometry. Periodic boundary condition was used in the spanwise direction. Different spanwise extents were used in this study i.e. 5%c, 10%c and 20%c. Results of different domain extensions will be discussed in the subsequent sections. Figure 5 shows the comparison of different spanwise extents chosen in this study.

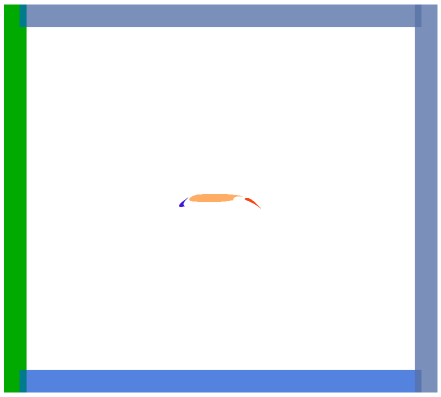

Fig. 4 Computational domain for high-lift simulation of F16 geometry.

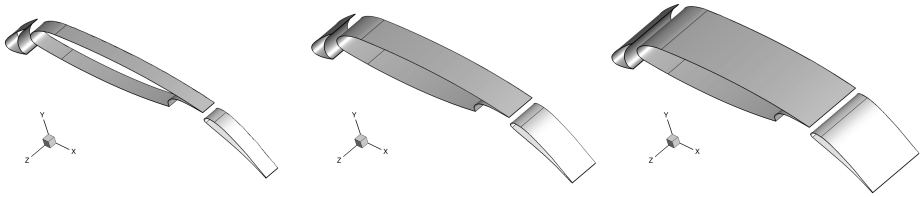

a) 5%c **b) 10%c** **c) 20%c**

Fig. 5 Spanwise extent comparison.

Instead of rotating the geometry, the inlet flow field was rotated at an angle of 6.15 deg. Iso-thermal LBE was solved with density $\rho = 1.20432\ kg/m^3$ and the physical speed of sound a_0=343.20 m/s.

Cartesian grid with the multiple refinement levels of isotropic, cubic elements is used for this simulation. Since the flow around the multi-element airfoil is highly unsteady, localised refinements are applied to the important flow regions i.e. slat cusp, slat and main element trailing edge etc. Figure 6 shows the close-up view of the slat cove and the flap cove region. The grid size of $\Delta x_f = 0.000125$ m (finest) is used for the localised refinement region. In order to accurately capture the recirculating flow in the slat and flap cove, the grid size in there is kept uniform. The grid refinement in the far-field is adjusted to resolve the acoustic waves up to the frequency f $\approx$ 11 kHz based on the spatial resolution requirement of 8 points per wavelength for LBM with HRR [19]. This grid refinement stretched from the axis origin of the F16 geometry until a distance of $\approx$ 3c in both horizontal and vertical direction. Grid size, $\Delta x = 0.004$ m, is kept uniform in this refinement region to accurately propagate acoustics in to the far-field. Details about the microphone arrangement in the far-field will be discussed in the later sections.

While using the periodic boundary there is a prerequisite that atleast two elements should be present, along the spanwise direction, in the coarsest level. Because of this prerequisite, isotropic mesh refinement and uniform mesh size used to resolve the acoustics in the far-field - direct propagation, the total number of grid nodes is higher. Table 1 gives the grid details for different spanwise extents.

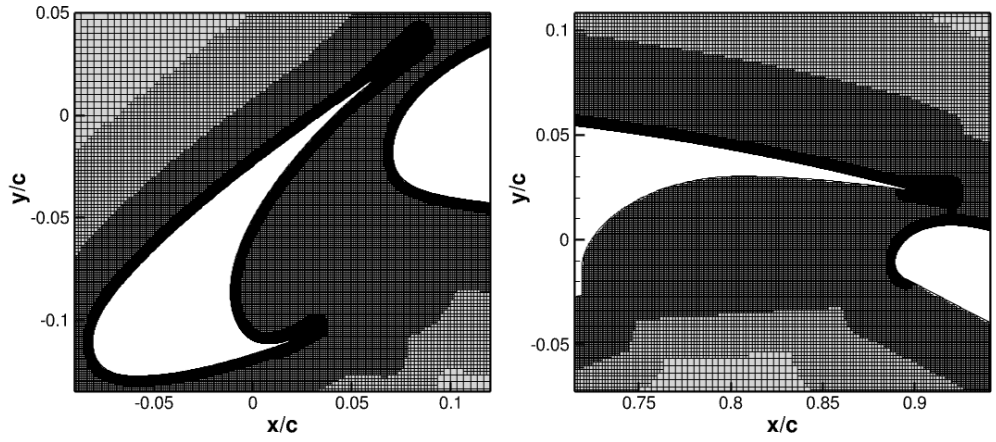

a) Slat cove **b) Flap cove**

Fig. 6 Close-up view of the grid in the slat and flap cove.

	≈ 5‰c	≈ 10‰c	≈ 20‰c
Spanwise extent (Δ_z) in m	0.016	0.032	0.064
Refinement Levels	7	8	9
No. of grid nodes (in million)	48	75	95

Table 1 Grid details for different spanwise extents.

C. Results

From this point onward the results of the ProLB simulations will be referred to as the WMLES results instead of WMLES-LBM results.

1. Steady flow

Results of the mean wall static pressure coefficient (C_p) for different spanwise extents were compared with the experimental results of F2 wind tunnel [13]. Spanwise extent of 20‰c showed better agreement with the experimental result. Thus, the C_p distribution is only shown for the 20‰c span. Figure 7a) shows the comparison of the C_p distribution obtained from the WMLES and the experimental result. Near the leading edge of the main element, unfortunately no experimental data for C_p was available as unsteady pressure was measured in that region. This is the region where the suction peak on the main element is observed i.e. $0.1 \leq \mathbf{x/c} \leq 0.2$, see figure 7a). In comparison with the experimental result, WMLES result show a higher value of suction peaks on the slat and flap. Apart from that, WMLES result for all three elements show a convincing agreement with the experimental result.

Figure 7b) shows the C_p distribution of the WMLES compared with the results of other scale resolving simulations (SRS). Results of these SRS were obtained from a comparative study conducted in the framework of European ARTEM project among the consortium partners (ONERA, Technical University of Braunschweig and DLR). FES [33] is based on the DLR CAA code PIANO [37] and Zonal DES (ZDES) [30], WRLES [32] results reported by ONERA. C_p distribution for the WMLES lies in between the distribution for the ZDES and WRLES which is an indication of a fairly good agreement with the other SRS results. Few differences in the C_p distribution were observed near the trailing edge of the flap between the experiment and WMLES result. Similar observation was also made by Terracol et al. [32]. Possible reason for the overprediction of the suction peaks can be a small separation occurring on the suction side of the flap trailing edge, in the experiment, which could affect the overall circulation around the airfoil [32].

Figure 8 shows the comparison of WMLES normalised mean velocity magnitude with the PIV measurements. Purpose for such a comparison is two-folds: First the flow on the suction side of the flap is massively separated in the PIV measurement but WMLES did not show any separation. The flow on the suction side of the airfoil appears to be more accelerated as compared to the PIV results. This observation is consistent with the higher suctions peaks observed

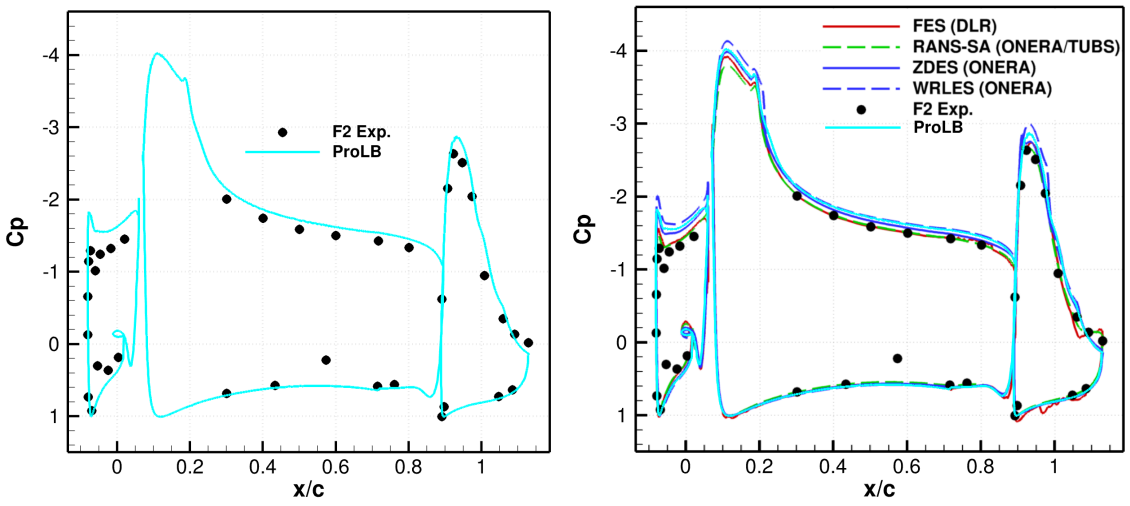

a) ProLB vs F2 **b) ProLB vs F2 & other SRS solvers**

Fig. 7 Static pressure coefficient (C_p).

in the figure 7.

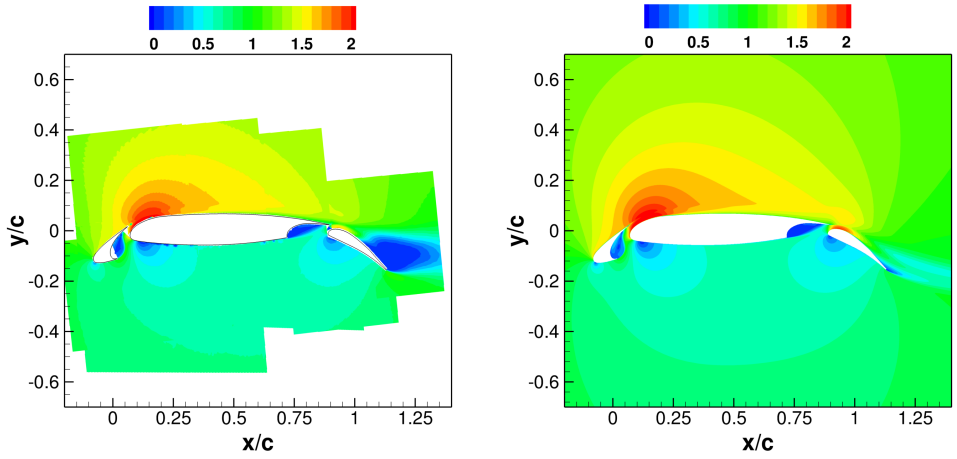

a) PIV **b) ProLB**

Fig. 8 Mean velocity magnitude comparison, normalised with U_∞.

The highly unsteady flow around the high-lift airfoil has to be resolved accurately for correct acoustic predictions. Importantly around the slat, as it has been cited as the main acoustic source of high-lift noise (see Ref.[[2]]). To verify the quality of the resolved flow, the flow statistics from the numerical simulation were extracted at several locations identical to the LDV measurement locations. The flow statistics were temporally averaged over 20 characteristic times i.e. $20c/U_\infty$. Normalized mean velocity magnitude and normalized turbulent kinetic energy (TKE) profiles of numerical simulations have been extracted from the slat cove at chosen locations as shown in figure 9.

In figure 9a) we see a recirculation bubble in the slat cove region. This bubble is enclosed by an unsteady shear layer that evolves from the slat cusp till it reattaches with the upper slat cove region near the slat trailing edge (TE). This unsteadiness in the shear layer develops due to interaction of the slow moving fluid in the recirculation bubble and the faster moving fluid around the bubble and passing through the slat gap.

The averaged flow statistics for different spanwise extents were compared with each other and also with the experimental results. Mean velocity and TKE profiles of 20%c showed better agreement with the experimental results and thus

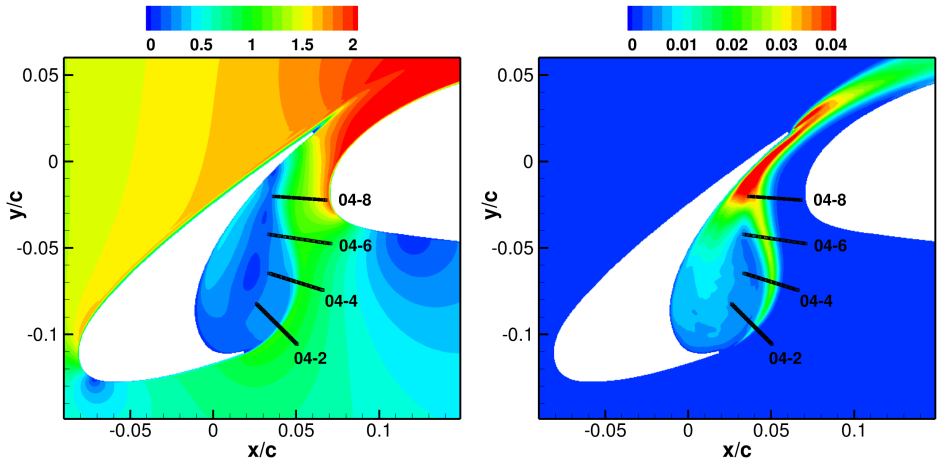

a) Velocity magnitude, normalised with U_∞ **b) 2D TKE, normalised with U_∞^2**

Fig. 9 Position of rakes from LDV measurement in the slat cove.

comparative results of only 20%c with the experiment are shown and discussed here. Figure 10a) - d) shows the comparison of numerical mean velocity magnitude profiles with the experimental results. Looking at the comparison of the velocity profiles, the thickness of the shear layer appears to be well reproduced at all the rakes. At the rake near the slat cusp, the position of the shear layer in the numerical profile appears to be slightly shifted along the downstream direction. It appears that the interaction between the shear layers originating from the top and bottom surfaces of slat cusp happens at a later point in time when compared to the experiment. Manoha et al. [32] mentioned that the transition of the shear layer near the slat cusp is expedited because of the residual freestream turbulence present in the wind tunnel. A much better agreement with the experimental profile, in terms of shear layer position, is observed as we move along the shear layer. In order to improve the shifted position of the shear layer near the slat cusp, see figure 10a), a finer mesh is required near the slat cusp. The WMLES profiles showed an overall good agreement with the experimental profiles.

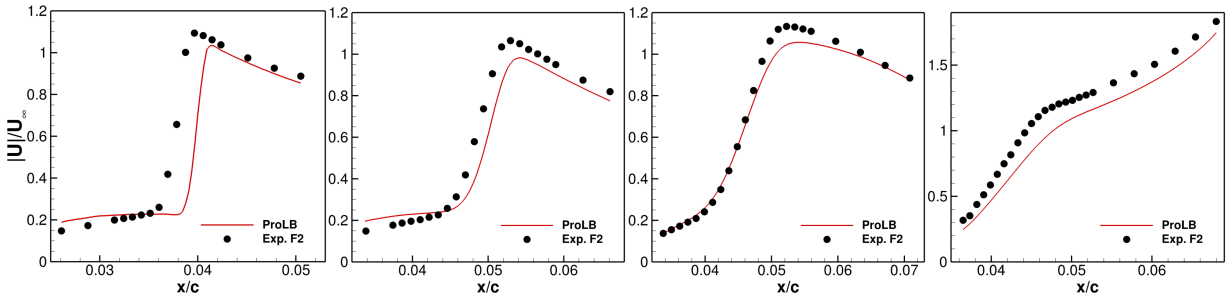

a) 04-02 **b) 04-04** **c) 04-06** **d) 04-08**

Fig. 10 Comparison of numerical mean velocity magnitude profiles with the LDV measurement in the slat cove.

Figure 9b) shows the 2D TKE contour in the slat cove. TKE in 2D is computed as: $k_{2D} = 0.5\,(U'^2_{RMS} + V'^2_{RMS})$ where U'^2_{RMS}&V'^2_{RMS} are the resolved root mean square velocity fluctuations in the streamwise and wall normal direction. Figure 11a)-d) shows the comparison of the numerical TKE profiles with the experimental results. Near the slat cusp (see figure 11a)), the numerical TKE profile is shifted in comparison with the experimental profile. But the agreement, in terms of the profile position, improves as we move along the downstream rakes. As for the velocity profile, this initial shift can again be associated with the late interaction of the shear layers from the top and bottom surfaces of the slat cusp. This late interaction causes a delayed development of unsteadiness and eventually a delayed transition to a fully turbulent shear layer. Effect of it can be seen in the underprediction of the peak TKE, near the slat cusp, and an subsequent overprediction of the peak TKE along the downstream locations. The form of the TKE profiles are recovered

decently but to get a more accurate agreement with the experimental results a finer mesh resolution is necessary near the slat cusp region.

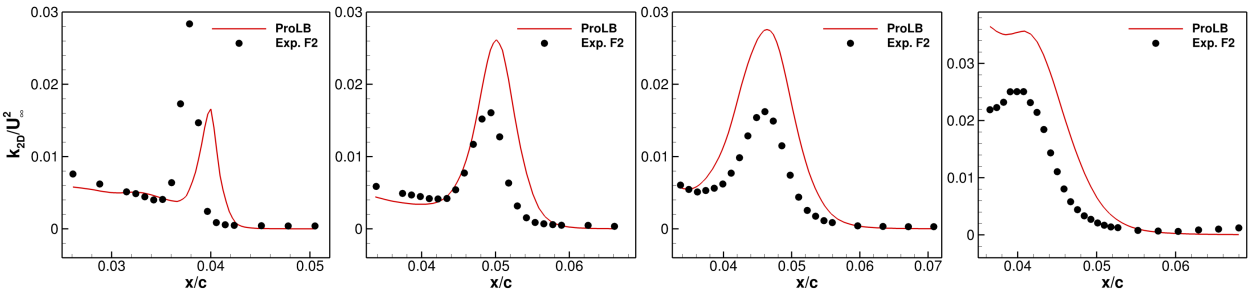

Fig. 11 Comparison of numerical 2D TKE and the LDV measurement in the slat cove.

2. Instantaneous flow

A close-up view of the flow inside the slat cove is shown in the figure 12 using the iso-surface of the normalised Q-criteria. It can be seen that the shear layer originating from the slat cusp breaks up in to 2D structures which gradually disintegrate further along the shear layer trajectory in to 3D structures until the impingement point, slightly upstream of the upper slat TE. At the impingement point, a portion of the vortical structures is convected further downstream and the other portion of the structures get re-ingested in to the recirculation bubble which later on enters into the shear layer. As a result of the flow acceleration in the slat gap, the structures convected downstream appear elongated along the flow direction. Besides the flow dynamics, presence of 2D and quasi-2D structures near the slat cusp indicates a slower development of unsteadiness in the shear layer. This appears to be the reason for the lower peak value in the numerical TKE profile, see figure 11a). Delayed development of unsteadiness results in a delayed disintegration of the spanwise vortical structures to 3D structures and this is the possible cause of higher peak values in the numerical TKE profiles, see figures 11b)-d). Similar observation about the shear layer development can be drawn from the iso-surface of normalised vorticity magnitude, see figure 13a). Flap cove has flow dynamics similar to that in the slat cove where the recirculation region is enclosed by a shear layer. From the iso-surface of vorticity magnitude (see figure 13b)) more 2D structures can be seen in the shear layer. This shear layer re-attaches with the inner part of the flap cove near the main element TE. Also the elongated streamwise-oriented vortices can be seen getting convected further downstream with the flow.

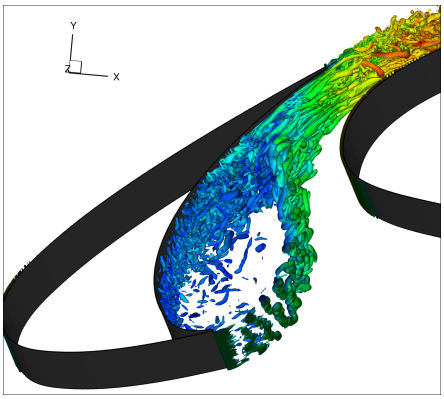

Fig. 12 Instantaneous slat cove flow(3D) represented with iso-surface of Q-criteria, $Q^*(Qc^2/U_\infty^2)$=10,000, coloured with the velocity magnitude.

Impingement of the shear layer on the pressure side of the slat is an important noise source and plays a major role in the acoustic feedback loop mechanism in the slat cove [30]. WMLES surface pressure spectral density at the

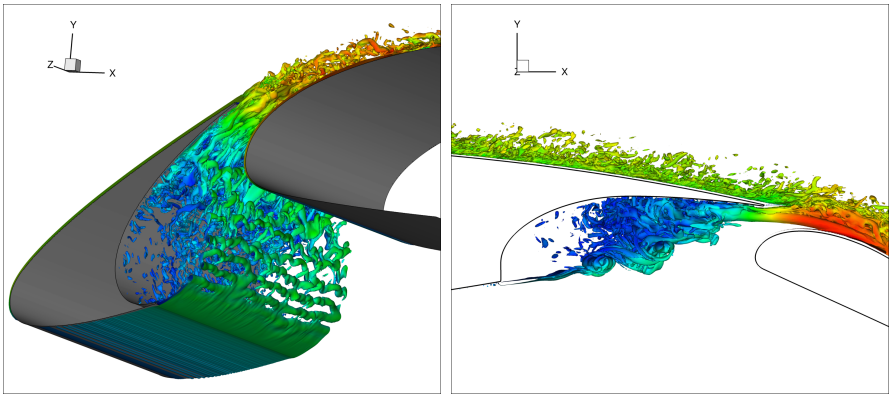

a) $\omega^*(|\omega|c/U_\infty)$**=250** **b)** $\omega^*(|\omega|c/U_\infty)$**=125**

Fig. 13 Instantaneous flow in slat & flap cove represented with iso-surface of vorticity magnitude, coloured with the velocity magnitude.

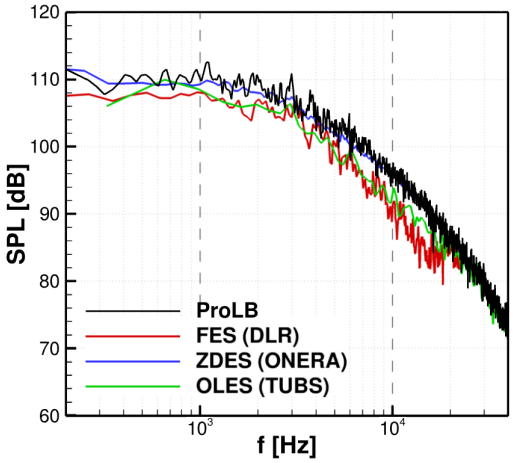

Fig. 14 Comparison of the narrow band spectra amongst different solvers. Measured at the impingement point in the slat cove.

impingement point is compared with the results from the previous studies with F16 wing geometry using continuum based solvers, see figure 14. OLES [34] is also based on DLR CAA code PIANO [37]. The WMLES spectra nicely fits the overall trend from all the other spectra and the agreement in the level can be observed over the entire frequency range. WMLES result almost overlaps the ZDES result indicating a similar degree of turbulence in that region.

3. Far-field acoustic propagation

Acoustic waves were directly resolved up to a distance of ≈ 1m, from the axis origin, in the far-field. Figure 15 shows the waves propagating in the far-field. On the suction side of the wing, high frequency pressure fluctuations emanating from the turbulence in the boundary layer are observed. These pressure fluctuations dissipate within a certain distance from the wing as the mesh resolution coarsens away from the wing. Also, the pressure fluctuations that represent the turbulent structures in the slat and flap cove, suction side of the wing and in the wake behind the flap can be seen. Low frequency waves originating from the slat and the flap cusp can be seen propagating towards the far-field.

To perform the acoustic analysis several microphones were placed in the near-field, inside and around the slat & flap cove, and in the far-field. Only the results of the microphones placed in the far-field will be shown and discussed. Figure 16a) shows the arrangement of the microphones in the far-field with respect to the high-lift wing. The microphones are positioned at locations similar to the AWB-measurements (shear corrected microphone positions, see [13]). Out of all the microphones shown in figure 16, we will only show the results for the microphone number 5. Figure 16b) shows

Fig. 15 Instantaneous sound pressure field, -20 to 20 Pa.

the comparison of the computed pressure spectra, between different spanwise extents, at microphone number 5 (see figure 16a). Following the Welch's procedure, the measured pressure signal is segmented in to six blocks with 50% overlap and Hanning windowed to compute the power spectral density (PSD) at microphone 5. The comparison of the pressure spectra do not show any major change in the features except the tonal peaks appear amplified with the increase in the span size. Slight changes in the broadband peaks were also observed. Slope of the spectra for the different span size agree well with each other besides a 2-3 dB visible shift in the level for the 5%c span. Noticeable are the tonal peaks at the frequencies f ≈ 850 & 1250 Hz. Initial investigation suggests that these tonal features in the spectra appears to have a source present in the flap cove. Similar observation was also made by Lockard et al. [36] on a 30P30N high-lift device. Impingement of the shear layer at the inner part of the flap cove and an interaction of the elongated streamwise oriented vortical structures with the leading edge portion of the flap, see figure 13b), results in some sort of acoustic feedback loop phenomenon in the flap cove. This aspect has to be further investigated.

Since we utilise a small domain width, compared to the experiment, with periodic boundaries we have to correct the spectra for the simplifications used in the computation. To compare the results of the simulation with the results of experiment, a 3D periodic slice to a 3D unbounded slice sound pressure correction is applied first (see the discussion in the Appendix A and B):

$$SPL_{3D,\Delta_z} = SPL_{3D,slice} + 10\log_{10}\left(\frac{\Delta_z^2\,\mathrm{f}}{a_0\,r}\right), \tag{23}$$

where r is the distance to the microphone. Secondly, to account for the sound radiation from the full span of the domain we apply the correction as specified by Kato et al. [35]:

$$SPL_{3D,L_z} = SPL_{3D,\Delta_z} + 10\log_{10}\left(\frac{L_z}{\Delta_z}\right). \tag{24}$$

Comparison of the corrected spectra with the experiment for different span size is shown in the figure 17. At this point it is important to notify that the experimental spectrum is also corrected in dB level as we use the shear corrected microphone locations, see [13]. Figure 17a) shows the comparison of the corrected computed spectrum with the corrected experimental spectrum for a span size of 5%c. The experimental spectrum is characterized by the tonal features which might be a result of an acoustic feedback mechanism in the slat cove [30]. The grey box is representative of the region where the comparison between experimental and numerical results cannot be done fairly as below 1000 Hz the experimental measurements have influence of the background noise i.e. reflection from the end-plates, measurement rig vibration etc. Low-frequency tones (f ≈ 850, 1250 Hz) are not observed in the experimental spectrum. In the

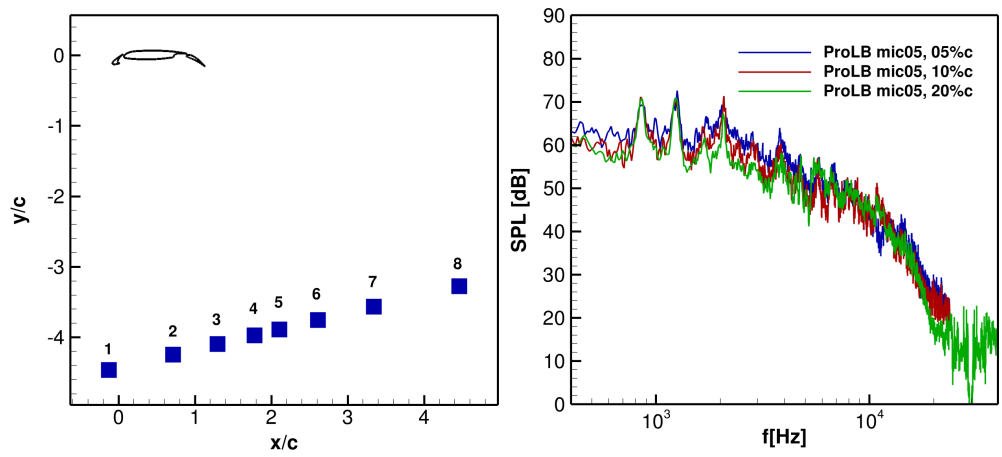

a) Microphone positions **b) Comparison of PSD at microphone 5**

Fig. 16 Far-field microphone arrangement and comparison of spectra between different spanwise extents.

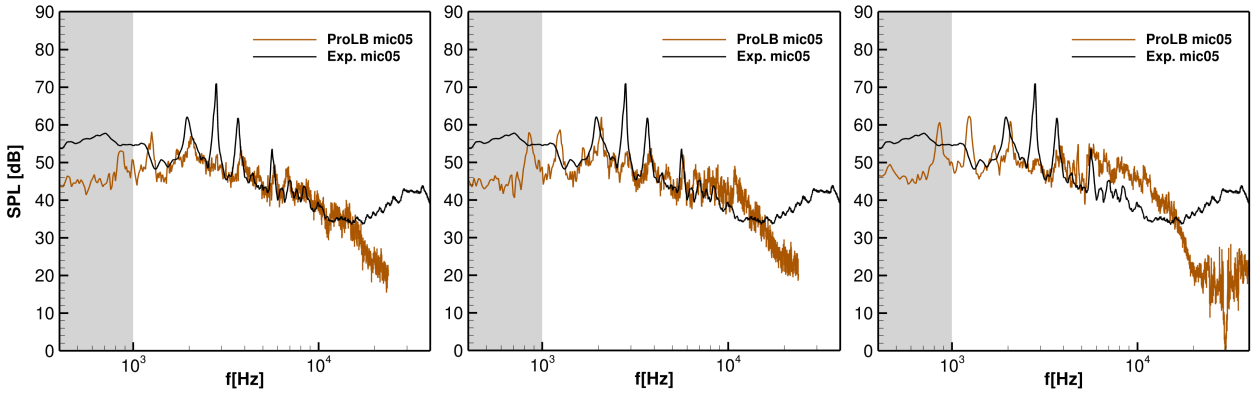

a) 5%c **b) 10%c** **c) 20%c**

Fig. 17 Comparison of experimental spectrum with computed spectrum (corrected) for different spanwise extents.

mid-frequency (f = 1000 - 10,000 Hz) region, the slope of the computed spectrum fits perfectly well with the slope of the experimental spectrum. Spectrum roll-off is observed around f ≈ 12,000 Hz. Focusing on the tonal features of the measured spectrum, broadband peaks are observed in the computed spectrum located more or less at the same frequencies. Presence of these broadband peaks indicate an existing potential for the tones to be recovered by fine tuning the computational setup i.e. finer mesh, longer signal sampling time etc.

Figure 17b) shows the comparison of the experimental vs. numerical spectra for the 10%c span size. As was observed for the 5%c span, the slope of the computed spectrum for 10%c span fits well with the experimental spectrum. Peak values for the low-frequency tones look amplified compared to the tonal peaks in 5%c span. The broadband peaks present in the mid-frequency region also look amplified as compared to broadband peaks in the 5%c span. Also the comparison with the tones present in the experimental spectrum look better. At f ≈ 10,725 Hz a sharp peak is observed. This frequency corresponds to an acoustic wave with wavelength exactly equal to the spanwise extent of the periodic domain (10%c). Periodicity causes a flow behaviour like in a duct i.e. cut-on mode at $f_1 = a_0/\Delta_z = 10{,}725$ Hz. It forces the waves below this frequency to be two-dimensional (Lockard et al. [36], also see the discussion in Appendix C).

Figure 17c) shows the comparison of the experimental vs. numerical spectra for the 20%c span size. Low-frequency tones have even higher peak values than the peak values observed for 10%c span. In the mid-frequency region the slope of the computed spectrum fits well with the experimental spectrum until f = 5,362 Hz. As observed for the 10%c span, this frequency corresponds to an acoustic wave with wavelength exactly equal to the spanwise extent of the periodic

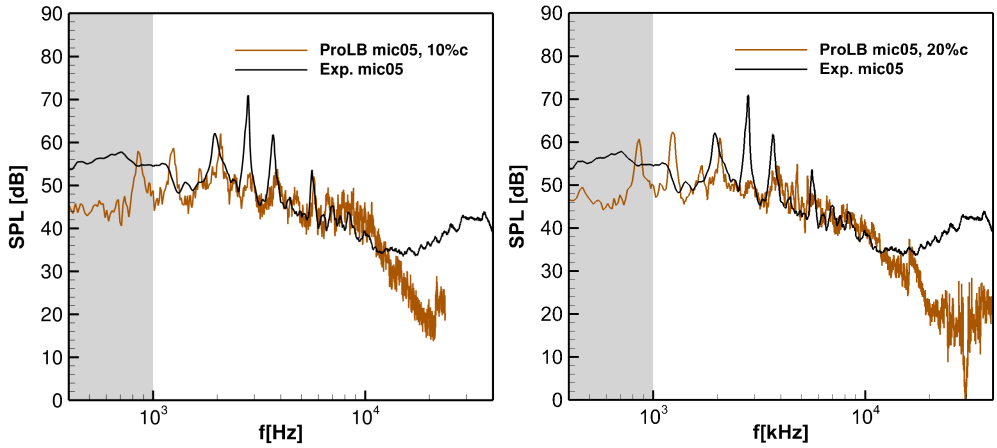

a) Spanwise extent 10%c **c) Spanwise extent 20%c**

Fig. 18 Shifted spectra comparison between different spanwise extents.

domain (20%c) i.e. f_1 = 5,362 Hz. From figure 17b) & c), we can observe that the the cut-on mode moves toward the lower frequencies with the increase in the spanwise extent. In this case, we not only see the cut-on mode but also the harmonics of it at frequencies f = 10,725 and 16087.5 Hz. Onset of this cut-on mode and its harmonics introduces additional energy at frequencies higher than the cut-on frequency and thus the level of the spectra have to be corrected by shifting it according to the jump present at the cut-on frequency. Figure 18 shows the comparison of the shifted spectra with the experimental results for different span size. In figure 18a), the level of the spectrum is shifted by -6 dB after the cut-on mode i.e. f_1 = 10,725 Hz. In figure 18b), the level of the spectrum is shifted by - 6 dB after f_1 = 5,362 Hz until the first harmonic at f = 10,725 Hz. From the first harmonic (f = 10,725) onward the spectrum level is shifted by - 8 dB until the second harmonic (f = 16087.5 Hz). Resulting slope of the spectra, in figure 18, matches very well with the experimental results over the entire mid-frequency range.

IV. Turbulent channel flow

Validation of the wall model implemented in Musubi was carried out with a 3D bi-periodic turbulent channel flow (TCF) test-case. Channel is periodic in the streamwise (X-axis) and spanwise (Z-axis) direction with two parallel walls along the wall normal direction (Y-axis). The domain size of the channel was chosen as 8πH x 2H x 3πH, which is similar to the reference DNS results of Moser et al. [39], where H = 1 m is the half channel height. Friction Reynolds number Re_τ = 1000 was chosen for this study, where Re_τ is defined as:

$$Re_\tau = \frac{\mathrm{H}u_\tau}{\nu}. \tag{25}$$

Wall model b.c was used at the boundaries normal to the wall-normal direction (Y-axis) and periodic b.c was used for the streamwise and spanwise domain direction (X- & Z-axis resp.). Volume forcing was used to drive the flow in the channel along the streamwise direction. Forcing scheme as mentioned in [29] was used:

$$F = \frac{\langle u_\tau^2 \rangle}{\mathrm{H}} + (U_b - \langle U \rangle)\frac{U_b}{\mathrm{H}}, \tag{26}$$

where $\langle \cdot \rangle$ indicates spatial averaging, U_b is the bulk velocity obtained from the DNS result [39], U is the computed instantaneous streamwise velocity. The flow was initialised with a power-law profile (see [27]) superimposed with turbulence fluctuations that were generated by random numbers of amplitude 5% U_b. Fluctuations were introduced to accelerate the onset of turbulence near the wall.

WMLES simulations are carried out using the Musker wall function with MRT collision operator. Uniform Cartesian mesh was used for the simulation. Care was taken to ensure that the flow achieves a statistically steady state before any data was sampled. The variables sampled were first temporally averaged and then averaged over the space. Quantities

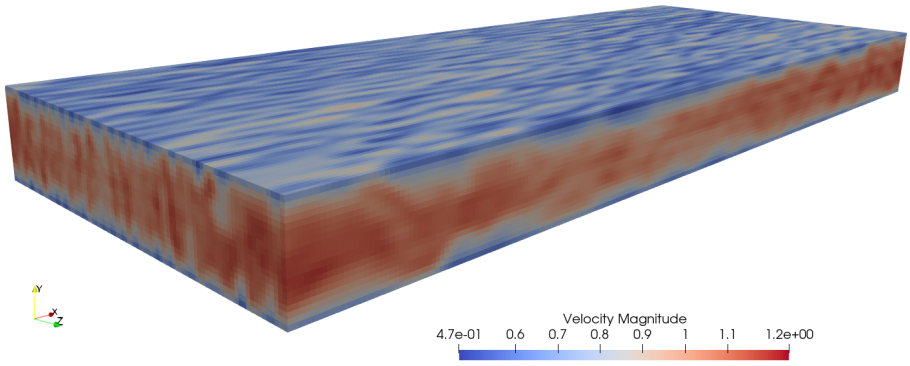

Fig. 19 Instantaneous velocity field.

used in comparing the results are mean streamwise velocity and shear stress. Mean streamwise velocity in viscous units is defined as: $U^+ = U/u_\tau$. Shear stress is computed as follows:

$$\langle u'v' \rangle = \langle UV \rangle - \langle U \rangle \langle V \rangle, \tag{27}$$

where U, V are the streamwise and the wall normal velocity components and u', v' are the streamwise and wall normal velocity fluctuations. In this study only the results of grid resolution with 20 points along the channel height i.e. $\Delta y^+ = 50$ is shown.

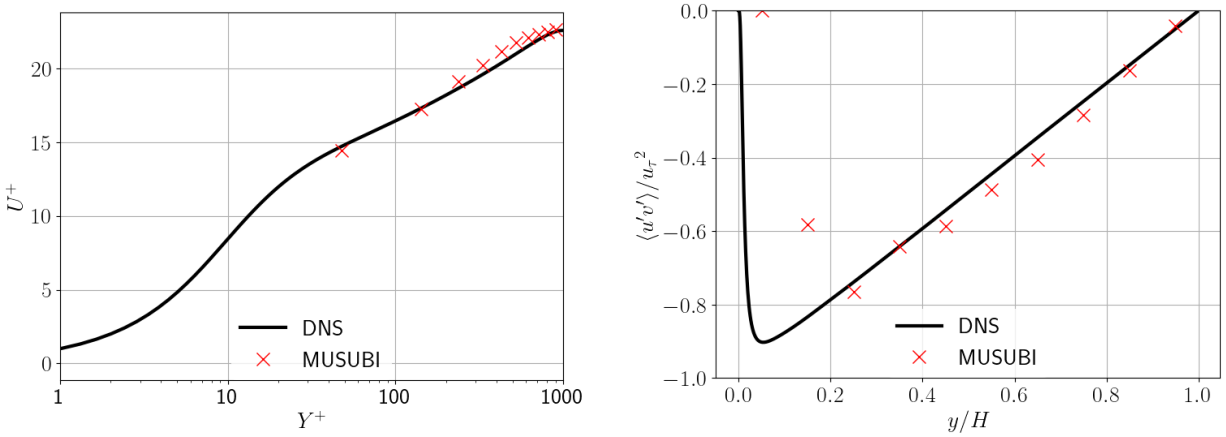

a) Normalized mean velocity **b) Normalized shear stress**

Fig. 20 Comparison of the time and space velocity and shear stress profiles with the DNS results.

The flow was allowed to develop over 30 channel flow passes i.e. $8\pi \mathrm{H}/U_b$. Once the steady state was achieved the data was sampled for over 400 flow passes. This also includes temporal and spatial averaging. Figure 19 shows a instantaneous, fully developed velocity flow field in the channel. Figure 20 shows the comparison of the mean velocity and shear stress profiles with the reference DNS results. The computed mean velocity profile has decently recovered the log-layer profile and is in good agreement with the reference result. Although the peak in the shear stress profile is slightly shifted towards the right, the shape of the DNS profile is well recovered. Overall the mean velocity profile shows a good agreement with reference DNS results and so does the shear stress profile.

V. Summary & Conclusions

This study was aimed at using WMLES-LBM as DNC tool for high-lift wing. Our approach involved two different aspects: application and understanding. In the application aspect, ProLB was used to simulate a high-lift wing with a limited spanwise extent. Periodic boundaries were applied along the span. Three different spanwise extents viz. 5%c, 10%c and 20%c were used. C_p distribution for WMLES showed a very nice agreement with the experimental results and also with the results of European ARTEM project. Results of the near-field averaged flow statistics were compared among different spanwise extents and also with the experimental results. In comparison to other spanwise extents, spanwise extent of 20%c showed better agreement with the experimental results. Thus only a comparison of flow statistics for 20%c span with the experimental results was shown. The mean velocity profiles showed a nice agreement with the experimental results except for some deviation near the slat cusp. TKE profiles very well recovered the profile shape when compared with the experimental results, but showed some deviations near the cusp and also in the peak TKE values. Looking at the development of the instantaneous flow structures in the slat cove, it was clear that those deviations can be reduced by improving the mesh near the slat cusp area. Comparison of the computed surface pressure spectrum, at the impingement point, with the results of European ARTEM project studies showed a very nice agreement in terms of the broadband content and the overall level of the spectra.

To the authors knowledge, no study (with F16) has been previously reported in the literature that deals with the direct evaluation of the acoustics from the LES domain with a limited spanwise extent. Pressure spectrum computed from the microphone located in the far-field was first corrected to account for a full 3D acoustic source (see Appendix A and B) and then corrected to account for the full spanwise extent L_z (see Kato [35]). After both the corrections were applied to the pressure spectrum, the corrected spectrum belonging to each spanwise extent was individually compared with the experimental spectrum. Interesting observations were made from this comparison. Periodicity introduced a duct like behaviour at frequency (f_1, cut-on mode) that correspond to the acoustic waves with wavelength equal to the spanwise extent of the periodic domain. At the frequency f_1, a jump was observed in the spectra and f_1 moved towards the lower frequency region with the increase in the spanwise extent. For the 20%c span, harmonics of f_1 frequency were observed. The increase in the spectral energy due to periodicity was corrected in the spectra for 10%c and 20%c. After that the slope of these corrected spectra fits very well with the experimental spectrum. Visually comparing the corrected spectra (see figure 17a) and figure 18), only the improvement in the low-frequency tones (f $\approx$ 850, 1250 Hz) was observed as the the spanwise extent was increased. Broadband content more or less remained the same with the change in the span size. Also, increase in the spanwise extent did not help to recover the tones that are visible in the experimental spectrum. But the presence of broadband peaks in the computed spectra presents a potential to recover the tones. This can be achieved by improving the mesh resolution in the slat cove region.

Finally, looking at the results in the near-field, where a fairly good agreement with the F2 experimental results for the C_p distribution and averaged flow statistics was observed, and in the far-field, where very nice agreement with the AWB experimental results was seen for the corrected far-field pressure spectra, ProLB showed its capability to be used as a DNC tool.

Future work will focus on improving the accuracy of the TKE profiles and recovering the missing tones in pressure spectrum by using a finer mesh resolution in the slat cove region. On the understanding part, nice results were observed for TCF with the current implementation. Next steps will involve a hierarchical mesh study for the current and higher Re_τ along with further development of the wall model for the curved boundaries.

Appendix

A. Sound pressure level scaling for sliced LES domain

The simulation utilizes a spanwise slice of limited extension with periodic boundary conditions. The spanwise extent is envisaged to be large enough to capture the spanwise coherence length scales in the resolved frequency range of the turbulent sound sources. For low to moderate Mach number problems, the spanwise domain extension is smaller than the acoustic wave length for most resolved frequencies. Due to the spanwise periodicity in the z-direction, sound waves are trapped in the resolved slice and sound propagation will become inherently two dimensional at sufficient distance to the source (refer also to the discussion in Appendix C).

That is, in the slice center plane at $z = 0$, sound waves from a single source located at coordinates $\boldsymbol{x}_s = (x_s, y_s)^T$ in the 2-D plane will exhibit a radial asymptotic decay-law with $1/\sqrt{r}$ based on a radial coordinate defined by $r = \sqrt{|\boldsymbol{x} - \boldsymbol{x}_s|}$, $\boldsymbol{x} = (x, y)^T$.

The asymptotic 2-D sound propagation requires a specific 2-D -to- 3-D correction to correct for the sound levels that

otherwise would obtained for unconfined 3-D sound propagation. Here, we apply the sound pressure level correction as discussed in Ref. [40] for flat plate trailing edge noise simulated on a 3-D LES slice.

A similar situation arises in the present context if we assume the sound problem to be dominated by edge source mechanism, e.g. trailing edge noise predominantly generated at or in the vicinity of the trailing edge of the slat.

For the present problem, the dominant edge sound source is located at an edge extending in spanwise z-direction. The edge position in the 2-D x-y-plane is defined by $\boldsymbol{x}_s = (x_s, y_s)^T$. The effect of the turbulent flow at the edge is assumed to be describable by an effectively resulting edge source $q(\boldsymbol{x}_s, z, \omega)$, refer also to the discussion in Ref. [43]. The average of the source over a spanwise extend of the slice ranging from $-\Delta_z/2$ to $\Delta_z/2$ reads $\overline{q}(\boldsymbol{x}_s, \omega) = \Delta_z^{-1} \int_{-\Delta_z/2}^{\Delta_z/2} q(\boldsymbol{x}_s, z, \omega) \mathrm{d}z$.

Since the source is compact over width Δ_z, the 3-D sound pressure level at position defined by $\boldsymbol{x}$ and z is written as the product of the sound source and an edge source Green's function, $\widehat{p}_{3D}(\boldsymbol{x}, z, \omega) = \overline{q}(\boldsymbol{x}_s, \omega)\Delta_z \mathcal{D}(\theta, \varphi)\ \exp(ikR)/(4\pi R)$, where $\mathcal{D}(\theta, \varphi)$ denotes the asymptotic directivity with polar angle θ measured in the $x-y$-plane and φ given as an angle defined by the spanwise displacement from $z = 0$, i.e. $\varphi = \operatorname{arccot}(z/r)$ and $R = \sqrt{r^2 + z^2}$. Due to symmetry reasons the directivity peaks at $\varphi = \pi/2$. Furthermore, the wave number can be expressed in terms of angular frequency $\omega = 2\pi \mathrm{f}$ and speed of sound a_0, i.e. $k = \omega/a_0$. For example, an according edge-source Green's function for flat plate trailing edge has been proposed by Howe [41].

The asymptotic sound field of a 2-D sound source at position $\boldsymbol{x}_s$ to an observer at $\boldsymbol{x}$ can be computed assuming a 3-D setup with infinitely extended coherent sound source along the z-direction of strength $\overline{q}(\boldsymbol{x}_s, \omega)$. Integrating the source with the 3-D edge-noise Green's function all along the span for observer positions at $z = 0$ and radial distance r to the edge yields a 2-D solution for the 2-D plane at $z = 0$.

Hence, $\widehat{p}_{2D} = \int \overline{q}(\boldsymbol{x}_s, \omega)\mathcal{D}(\theta, \varphi)\ \exp\left(ik\sqrt{r^2 + z'^2}\right)/(4\pi\sqrt{r^2 + z'^2})\mathrm{d}z'$. Assuming large but finite distance r, a method of stationary phase argument then provides an asymptotic solution to the integral, which after rearrangement and substitution part of the resulting expressions by the results for $\widehat{p}_{3D}(\boldsymbol{x}_s, z = 0, \omega)$, eventually reads

$$\widehat{p}_{3D}(\boldsymbol{x}_s, 0, \omega) = \widehat{p}_{2D}(\boldsymbol{x}_s, \omega)\ \frac{1+i}{2}\sqrt{\frac{\omega\Delta_z^2}{a_0 \pi r}}. \tag{28}$$

The sound pressure fluctuations resulting from the turbulent edge noise sources are assumed to be statistical stationary and exhibiting a finite integral time scale. Hence, the double sided power spectral density $S_{pp}(\mathrm{f})$ infers from the Fourier transform of fluctuating pressure via [42]

$$S_{pp}(\mathrm{f}) = \lim_{T \to \infty} \left[\hat{p}(\omega)\hat{p}^*(\omega)\right], \tag{29}$$

where the asterisk indicates the conjugate complex and T is the time extend of the pressure sample from which the Fourier transform is derived. Upon identifying the 2-D solution in Eq. (28) with the asymptotic pressure solution obtained for a 3-D sliced domain and using the previous result, the corrected power spectral density infers as

$$S_{pp}(\mathrm{f})_{3D,\Delta_z} = S_{pp}(\mathrm{f})_{3D,slice}\left(\frac{\Delta_z^2 \mathrm{f}}{a_0\, r}\right). \tag{30}$$

The evaluation of e.g. narrow band sound pressure levels eventually yields

$$SPL_{3D,\Delta_z} = SPL_{3D,slice} + 10\log_{10}\left(\frac{\Delta_z^2 \mathrm{f}}{a_0\, r}\right), \tag{31}$$

where $SPL_{3D,slice} \simeq 10\log_{10}\left(\frac{S_{pp}(\mathrm{f})\Delta \mathrm{f}_B}{p_{ref}^2}\right)$, with $p_{ref} = 2 \cdot 10^{-5}\mathrm{Pa}$ and using $\Delta \mathrm{f}_B = 1\mathrm{Hz}$.

B. Further discussion of 3-D slice correction

Note, the 3-D slice correction already incorporates the spanwise coherence length scale as being present in the effective turbulent edge source. In Ref. [43] a 2-D -to- 3–D correction has been proposed that assumes a setup, where sound sources are computed with turbulent quantities taken from a 2-D slice (x-y-plane) extracted from the 3-D turbulent field. These extracted sound sources are used with a 2-D computational aeroacoustics (CAA) propagation method. In this case information has to be included about the spanwise coherence of the sound sources for sound pressure level

correction. In Ref. [43] the coherence model Amiet [44] has been adopted. In what follows, the 2-D -to- 3-D correction as derived in Ref. [43] for such a setup does not exhibit a frequency correction, i.e. only a level correction is applied and the shape of the uncorrected spectra already coincides with those of the corrected spectra.

In contrast, the 3-D slice correction applied here implicitly incorporates the spanwise coherence length scale as being simulated as part of the LES and has not to be modeled. In consequence, the correction as given by Eq. (31) involves a frequency dependence, i.e. the corrected sound spectra exhibit a modified slope with additional 3dB/octave increase relative to the uncorrected spectrum.

To see that the averaged source as introduced in the previous section already includes the spanwise coherence information, one can consider the sound field that results at a given observer position (r, z) from a suitable edge-source distribution and edge-source Green's function,

$$\widehat{p}_{3D}(r, z = 0, \omega) = \int_{-\Delta_z/2}^{\Delta_z/2} G_{3D}(r, z - z', \omega) q(z', \omega) \mathrm{d}z'. \tag{32}$$

Here, $q(z', \omega)$ denotes the edge source. Assuming the source along the span to be acoustically compact, it is sufficient to evaluate the Green's function at one representative position, e.g. $z = 0$. Hence, it can be moved out of the integral, yielding the product of the spanwise averaged source with the 3-D Green's function as being used in the previous section,

$$\widehat{p}_{3D}(r, 0, \omega) = G_{3D}(r, 0, \omega) \overline{q}(\omega) \Delta_z, \quad \overline{q}(\omega) := \frac{1}{\Delta_z} \int_{-\Delta_z/2}^{\Delta_z/2} q(z', \omega) \mathrm{d}z'. \tag{33}$$

Consequently, the absolute value of pressure is given by

$$|\widehat{p}_{3D}|^2 = |G_{3D}|^2 \, |\overline{q}|^2 \, \Delta_z^2. \tag{34}$$

Alternatively, the square of the absolute value of pressure formally also follows from

$$|\widehat{p}_{3D}(r, z, \omega)|^2 = \widehat{p}_{3D} \widehat{p}_{3D}^* = \int_{-\Delta_z/2}^{\Delta_z/2} \int_{-\Delta_z/2}^{\Delta_z/2} G_{3D}(r, z - z', \omega) G_{3D}^*(r, z - z'', \omega) \, q(z', \omega) q^*(z'', \omega) \mathrm{d}z' \mathrm{d}z''. \tag{35}$$

The compactness argument allows to evaluate the Green's functions at representative position z, $z - z' \to 0$ and $z - z'' \to 0$, so that the Green's function can be moved out off the integral. The remaining term can be expressed in terms of the coherence function defined by

$$C_{qq}(z' - z'', \omega) := \frac{q(z', \omega) q^*(z'', \omega)}{|q(\omega)|^2} \tag{36}$$

Due to the homogeneity of the problem in spanwise direction the square of the source strength must not depend on the spatial coordinate. Due to the symmetry of the problem, spanwise two-point correlations are symmetric relative to z', i.e. the two-point correlations of the edge source is an even function. Therefore the above coherence function becomes a real function, refer to the discussion in Ref. [43]. Hence,

$$|\widehat{p}_{3D}(r, z, \omega)|^2 = |G_{3D}(r, 0, \omega)|^2 \, |q(\omega)|^2 \int_{-\Delta_z/2}^{\Delta_z/2} \int_{-\Delta_z/2}^{\Delta_z/2} C_{qq}(z' - z'', \omega) \mathrm{d}z' \mathrm{d}z''. \tag{37}$$

The integral with respect to z'' gives the coherence length scale $l_z(\omega) = \int C_{qq}(\zeta, \omega) \mathrm{d}\zeta$, which due to homogeneity is not a function of the spanwise coordinate. Hence, second integration with respect to z' yields Δ_z and

$$|\widehat{p}_{3D}|^2 = |G_{3D}|^2 \, |q(\omega)|^2 \, l_z(\omega) \Delta_z. \tag{38}$$

Comparison with Eq. (34) yields the relationship

$$|\overline{q}| = |q(\omega)| \sqrt{\frac{l_z(\omega)}{\Delta_z}}. \tag{39}$$

In other words, the averaged source term incorporates information about the local source strength and the coherence length scale $l_z(\omega)$ along the spanwise direction (normalized with the constant spanwise width) as resolved by the underlying scale resolving simulation.

C. Aeroacoustic cut-on effects visible in LES slice solution

A duct of plane walls in the z- and y-direction and width d_y and d_z as shown in figure 21 has cut-on frequencies given by [42]

$$\mathrm{f}_c = \frac{a_0}{2}\sqrt{\frac{m^2}{d_y^2} + \frac{n^2}{d_z^2}}. \tag{40}$$

For a LES slice of width Δ_z and periodic boundary conditions in the spanwise direction, this result can be adopted by making the replacements $\Delta_z \to d_z$, $d_y \to \infty$ and $2n_{periodic} = n$, hence

$$\mathrm{f}_c = n_{periodic}\mathrm{f}_1, \quad \mathrm{f}_1 := \frac{a_0}{\Delta_z}. \tag{41}$$

The extension in y-direction much larger than the slice width Δ_z (and an termination of acoustically transparant boundary conditions) motivates the limit $d_y \to \infty$. For solid walls, the fundamental duct solution infers by introducing cosine ansatz functions for the z-direction solution that furthermore satisfies the solid wall boundary condition at the wall, $\partial p/\partial z|_{wall} = 0$. This yields valid ansatz function where the spanwise width corresponds to a multiple of the half wave length, $n\lambda/2 = \Delta_z, n \in \mathbb{N}_0$. For the present case with periodic boundary condition, valid ansatz functions are potentially sine- and cosine-functions with wave length being a multiple of the domain width, $n_{periodic}\lambda = \Delta_z$, $n_{periodic} \in \mathbb{N}_0$. This motivates the last relation $n_{periodic} = 2n$.

Note, waves of mode order $n_{periodic} = 0$ are always cut-on. These represent plane-waves of arbitrary frequency traveling along the radial x-y-direction and motivate the 2-D correction discussed in the previous paragraphs. For the critical frequency f_1 further modes become cut-on. Similar to the simulation of wave-propagation in a wave-guide, the cut-on becomes visible in the resolved spectrum as a distinct saw tooth pattern. With increasing domain width, the first cut-on frequency shifts to lower frequencies and higher cut-on frequencies become potentially visible in the resolved frequency regime.

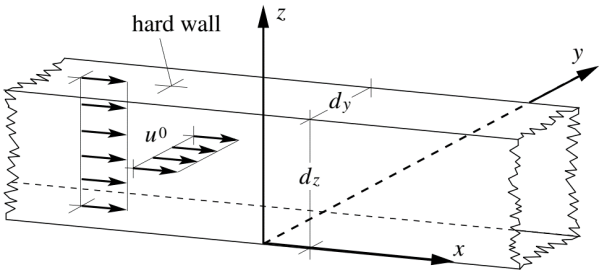

Fig. 21 Plane walls parallel duct from Ref. [42]

Acknowledgments

The first three authors would like to acknowledge the funding received in the framework of the German project INTONE (Minderung von Triebwerksinstallations- und Hochauftriebslaerm), LuFo V-3, Foerderkennzeichen FKZ 20A1703E. Part of this work received funding from the ARTEM project, European Union‘s Horizon 2020 research and innovation programme, grant No 769 350. Furthermore funding received as part of the DLR project NABLA (Numerical Aeroacoustics Based on LAttice Boltzmann). The authors also acknowledge the computational resources provided by the CARA cluster of the German Aerospace Center. Lastly, the authors would also like to acknowledge the CS GROUP for providing the ProLB v2.6.3 licenses and the ProLB consortium, in particular Alois Sengissen from Airbus, for their fruitful support of the high-lift device simulation activities.

References

[1] Dobrzynski, W., Ewert, R., Pott-Pollenske, M., Herr, M., and Delfs, J. (2008). Research at DLR towards airframe noise prediction and reduction. Aerospace Science and Technology, 12(1), 80-90.

[2] Dobrzynski, W. (2010). Almost 40 years of airframe noise research: what did we achieve?. Journal of aircraft, 47(2), 353-367.

[3] Rumsey, C. L., and Ying, S. X. (2002). Prediction of high lift: review of present CFD capability. Progress in Aerospace Sciences, 38(2), 145-180.

[4] Spalart, P. R. (1997). Comments on the feasibility of LES for wings, and on hybrid RANS/LES approach, advances in DNS/LES. In Proceedings of 1st AFOSR International Conference on DNS/LES, 1997.

[5] Choi, H., and Moin, P. (2012). Grid-point requirements for large eddy simulation: Chapman's estimates revisited. Physics of fluids, 24(1), 011702.

[6] Chen, S., and Doolen, G. D. (1998). Lattice Boltzmann method for fluid flows. Annual review of fluid mechanics, 30(1), 329-364.

[7] Piomelli, U., and Balaras, E. (2002). Wall-layer models for large-eddy simulations. Annual review of fluid mechanics, 34(1), 349-374.

[8] Larsson, J., Kawai, S., Bodart, J., Bermejo-Moreno, I.: Large eddy simulation with modeled wall-stress: recent progress and future directions. Mechanical Engineering Reviews, Vol. 3(1), 15-00418 (2016).

[9] Koenig, B., Singh, D., and Fares, E. (2018, September). Lattice Boltzmann high-lift simulations-a step beyond classical CFD. In 31st Congress of the International Council of the Aeronautical Sciences.

[10] Satti, R., Li, Y., Shock, R., and Noelting, S. (2008). Unsteady Flow Simulation of a High Lift Trapezoidal Wing Using Lattice Boltzmann Method. In 38th Fluid Dynamics Conference and Exhibit (p. 4145).

[11] Satti, R., Li, Y., Shock, R., and Noelting, S. (2008). Aeroacoustic Analysis of a High Lift Trapezoidal Wing using lattice Boltzmann Method. In 14th AIAA/CEAS Aeroacoustics Conference (29th AIAA Aeroacoustics Conference) (p. 3048).

[12] Manoha, E. and Pott-Polenske, M., Benchmark for Airframe Noise Computations - LEISA2 Category 6 - Low-Noise Exposure Integrated Design for Start and Approach Database Description - Version 1, 03.06.2014

[13] Manoha, E., and Pott-Pollenske, M. (2015). LEISA2: an experimental database for the validation of numerical predictions of slat unsteady flow and noise. In 21st AIAA/CEAS Aeroacoustics Conference (p. 3137)

[14] Khorrami, M. R., and Fares, E. (2016). Simulation-based airframe noise prediction of a full-scale, full aircraft. In 22nd AIAA/CEAS aeroacoustics conference (p. 2706)

[15] Krüger, T., Kusumaatmaja, H., Kuzmin, A., Shardt, O., Silva, G., and Viggen, E. M. (2017). The lattice Boltzmann method. Springer International Publishing, 10(978-3), 4-15.

[16] Shan, X., & He, X. (1998). Discretization of the velocity space in the solution of the Boltzmann equation. Physical Review Letters, 80(1), 65.

[17] www.prolb-cfd.com/

[18] Jacob, J., Malaspinas, O., and Sagaut, P. (2018). A new hybrid recursive regularised Bhatnagar–Gross–Krook collision model for Lattice Boltzmann method-based large eddy simulation. Journal of Turbulence, 19(11-12), 1051-1076.

[19] Astoul, T., Wissocq, G., Boussuge, J. F., Sengissen, A., & Sagaut, P. (2020). Analysis and reduction of spurious noise generated at grid refinement interfaces with the lattice Boltzmann method. Journal of Computational Physics, 418, 109645

[20] Leveque, E., Touil, H., Malik, S., Ricot, D., and Sengissen, A. (2018). Wall-modeled large-eddy simulation of the flow past a rod-airfoil tandem by the Lattice Boltzmann method. International Journal of Numerical Methods for Heat and Fluid Flow.

[21] Lévêque, E., Toschi, F., Shao, L., & Bertoglio, J. (2007). Shear-improved Smagorinsky model for large-eddy simulation of wall-bounded turbulent flows. Journal of Fluid Mechanics, 570, 491-502. doi:10.1017/S0022112006003429

[22] Hasert, M., Masilamani, K., Zimny, S., Klimach, H., Qi, J., Bernsdorf, J., and Roller, S. (2014). Complex fluid simulations with the parallel tree-based lattice Boltzmann solver Musubi. Journal of Computational Science, 5(5), 784-794.

[23] d'Humières, D. (2002). Multiple–relaxation–time lattice Boltzmann models in three dimensions. Philosophical Transactions of the Royal Society of London. Series A: Mathematical, Physical and Engineering Sciences, 360(1792), 437-451.

[24] Lallemand, P., & Luo, L. S. (2000). Theory of the lattice Boltzmann method: Dispersion, dissipation, isotropy, Galilean invariance, and stability. Physical review E, 61(6), 6546

[25] A. W. Vreman, "An eddy-viscosity subgrid-scale model for turbulent shear flow: Algebraic theory and applications", Physics of Fluids 16, 3670-3681 (2004) https://doi.org/10.1063/1.1785131

[26] Malaspinas, O., and Sagaut, P. (2014). Wall model for large-eddy simulation based on the lattice Boltzmann method. Journal of Computational Physics, 275, 25-40.

[27] Haussmann, M., Barreto, A. C., Kouyi, G. L., Rivière, N., Nirschl, H., & Krause, M. J. (2019). Large-eddy simulation coupled with wall models for turbulent channel flows at high Reynolds numbers with a lattice Boltzmann method—Application to Coriolis mass flowmeter. Computers & Mathematics with Applications, 78(10), 3285-3302

[28] Werner, H., Wengle, H.: Large-eddy simulation of turbulent flow over and around a cube in a plate channel. In Turbulent shear flows. Springer, Berlin, Heidelberg, Edn. 8, (1993).

[29] Cabrit, O., & Nicoud, F. (2009). Direct simulations for wall modeling of multicomponent reacting compressible turbulent flows. Physics of Fluids, 21(5), 055108

[30] Terracol, M., Manoha, E., & Lemoine, B. (2016). Investigation of the unsteady flow and noise generation in a slat cove. AIAA Journal, 54(2), 469-489

[31] Deck, S. (2005). Zonal-detached-eddy simulation of the flow around a high-lift configuration. AIAA journal, 43(11), 2372-2384.

[32] Terracol, M., and Manoha, E. (2020). Wall-resolved Large-Eddy Simulation of a three-element high-lift airfoil. AIAA Journal, 58(2), 517-536.

[33] Heitmann, D., and Ewert, R. (2019). Investigation of slat noise on high-lift configuration using active backscatter model in LES. In 25th AIAA/CEAS Aeroacoustics Conference (p. 2644).

[34] Bernicke, P., & Akkermans, R. A. D. (2021, May). Hybrid Overset-LES Simulations of Noise Reduction Concepts of Loaded Airfoils. In Journal of Physics: Conference Series (Vol. 1909, No. 1, p. 012004). IOP Publishing.

[35] Kato, C., Iida, A., Takano, Y., Fujita, H. A. J. I. M. E., & Ikegawa, M. (1993). Numerical prediction of aerodynamic noise radiated from low Mach number turbulent wake. In 31st aerospace sciences meeting (p. 145)

[36] Lockard, D. P., Choudhari, M. M., & Buning, P. G. (2014). Grid sensitivity study for slat noise simulations. In 20th AIAA/CEAS Aeroacoustics Conference (p. 2627)

[37] Delfs, J. W., Bauer, M., Ewert, R., Grogger, H. A., Lummer, M., and Lauke, T. G. (2008). Numerical Simulation of Aerodynamic Noise with DLR's aeroacoustic code PIANO.

[38] https://turbulence.oden.utexas.edu/

[39] Lee, M., & Moser, R. (2015). Direct numerical simulation of turbulent channel flow up to $Re_\tau \approx 5200$. Journal of Fluid Mechanics, 774, 395-415. doi:10.1017/jfm.2015.268

[40] Ewert, R. and Schröder, W., "On the simulation of trailing edge noise with a hybrid LES/APE method," Journal of Sound and Vibration, Vol. 270, No. 3, 2004, pp. 509–524.

[41] Howe, M. S., "Edge-source acoustic green's function for an airfoil of arbitrary chord, with application to trailing-edge noise," The Quarterly Journal of Mechanics and Applied Mathematics, Vol. 54, No. 1, 02 2001, pp. 139–155.

[42] Delfs, J., "Basics of Aeroacoustics," Lecture Notes, Technical University Braunschweig, 2017.

[43] Ewert, R., Appel, C., Dierke, J., and Herr, M., "RANS/CAA Based Prediction of NACA 0012 Broadband Trailing Edge Noise and Experimental Validation," 2009-3269, AIAA-Paper, May 2009.

[44] Amiet, R., "Noise due to turbulent flow past a trailing edge," Journal of Sound and Vibration, Vol. 47, No. 3, 1976, pp. 387–393.